Check for updates

Faceted wrinkling by contracting a curved boundary†

Anshuman S. Pal, [ID] [a] Luka Pocivavsek[b] and Thomas A. Witten*[a]

Single-mode deformations of two-dimensional materials, such as the Miura-ori zig-zag fold, are important to the design of deployable structures because of their robustness; these usually require careful pre-patterning of the material. Here we show that inward contraction of a curved boundary produces a fine wrinkle pattern with a novel structure that suggests similar single-mode characteristics, but with minimal pre-patterning. Using finite-element representation of the contraction of a thin circular annular sheet, we show that these sheets wrinkle into a structure well approximated by an isometric structure composed of conical sectors and flat, triangular facets. Isometry favours the restriction of such deformations to a robust low-bending energy channel that avoids stretching. This class of buckling offers a novel way to manipulate sheet morphology *via* boundary forces.

The flourishing field of extreme mechanics[4–7] seeks ways in which large, spontaneous material deformations yield robust, reproducible structures and motions. Many of these structures exploit the selective deformations shown by thin sheets, which bend or fold easily but resist internal stretching strongly.[8–19] The large resistance to stretching creates strong, non-local constraints that restrict the sheet to selected modes of deformation. A classic example is the Miura-ori folding pattern.[1,20,21] This periodic pattern enables one to contract a spread-out flat sheet of paper into a compactly folded state with one single mode of deformation dictated by the pattern (see Fig. 1a). Here we report similar robust deformation of a flat sheet without the position-dependent processing needed for an origami fold. Instead, we specify an initial annular shape and a simple mode of edge deformation: contracting the inner boundary radially. The result is a strongly reproducible three-dimensional pattern of high-amplitude wrinkles. We attribute the reproducibility to a qualitative feature of the simulated, finite-element simulation—each wrinkle approaches an isometric shape, with no stretching. This unstretched morphology is made possible by a distinct pattern of flat, triangular facets alternating with smoothly-curving conical segments.

We consider a minimal form of radial contraction that we call "inner Lamé" contraction. We displace the inner boundary of the annulus with no further constraints. Our interest in this

geometry arose from experiments on the curling of edge-connected polymeric sheets with unequal solvent swelling. Ref. 22 shows the result for two half sheets with different swelling separated by a straight boundary. We simulated the radial analogue of this situation, where the straight boundary was replaced by a circular boundary separating an inner region with little swelling from an outer one with more swelling. The swelling resulted in fine radial wrinkling like that shown in Fig. 1. The present simplified system was developed to understand this wrinkling.

As shown in Fig. 1c, the inner Lamé contraction produces fine wrinkling like the conventional Lamé contraction of Fig. 1b. However the two wrinkled states are radically different. The conventional Lamé wrinkle wavelength is explained in terms of the applied tension.[2] However, in the inner Lamé, the exterior tension of the Lamé state is absent, and so the established mechanism for the wrinkle wavelength cannot apply. Indeed, our wrinkling contrasts with most wrinkled systems, where the bending energy favoring longer wavelengths is countered by the energy associated with some external forcing.[9,23] The wrinkle wavelength then depends explicitly on the strength of this forcing. The inner Lamé system has no such strength parameter. Instead, the deformation is defined in terms of the geometric displacement of the inner edge only.

Even among geometrically-defined forms of wrinkling, the inner-Lamé geometry is anomalous. *A priori*, it doesn't conform to typical one-dimensional buckling treatable as an Euler elastica system.[24] Other forms in which the constraint is applied at one boundary[14,25] do not give a well-defined wave number as we find.

Furthermore, we note that the forms of wrinkling mentioned above are explained as equilibrium ground-states of

[a] *James Franck Institute and Dept. of Physics, University of Chicago, IL, USA.*
  E-mail: t-witten@uchicago.edu
[b] *Dept. of Surgery, Pritzker School of Medicine, University of Chicago, Chicago, IL,*
  USA
† Electronic supplementary information (ESI) available. See DOI: https://doi.org/10.1039/d3sm01347b
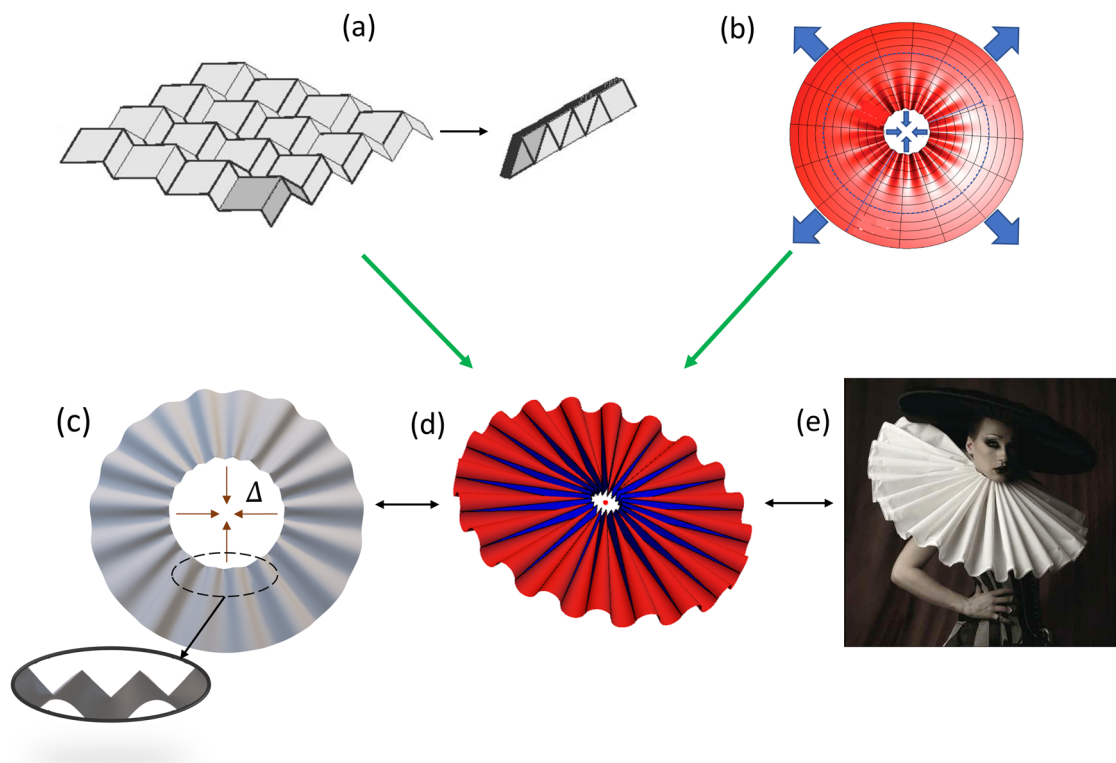
Fig. 1 Geometry-controlled robust radial wrinkling. (a) Miura-ori patterns guide a flat sheet to contract into a folded state with a single, continuous motion (adapted from ref. 1). (b) Smooth radial (*i.e.*, Lamé) wrinkling in an annulus under both inner and outer tension, indicated by arrows (adapted from ref. 2). In this paper, we study Miura-ori like robust deformation of an annulus in a radial Lamé setting. This deformation can be generated in multiple ways. (c) Finite-element calculated shape under uniform radial contraction of the inner boundary, described in Methods (inset shows detail of emergent zigzag inner boundary). (d) Circular-cone-triangle geometric construction defined in Section 2, with triangles shown in blue and cones in red. (e) Ruff collar garment (reproduced from ref. 3) made by manually pleating the inner boundary of an annular piece of cloth.

the system. In our system the wrinkles emerge from a quasi-static deformation. That is, the inner displacement is applied gradually, and the configuration is allowed to relax at every stage. This procedure corresponds to how one would perform the deformation experimentally. In this limit, the system follows a given energy minimum as the deformation is imposed. It need not be an energy ground state.

In this paper, we address the structure of the individual wrinkles resulting from this unusual mode of deformation.‡ We show that a strain-free isometric shape quantitatively accounts for observed features of our simulated shape, notably the elastic energy shown in Fig. 5. This energy contrasts strongly with the much higher energy expected with a simple sinusoidal wrinkling pattern (Section 3.3). Moreover, the simulated deformation matches an explicitly isometric deformation of the original annulus into a cone-triangle pattern. We describe the robustness of the structure using a variety of initial and boundary conditions for the contracted inner boundary. We argue that the observed robustness of the cone-triangle structure is a natural consequence of its isometric property. We note how the cone-triangle structure can be

induced *via* different paths, as illustrated in Fig. 1c–e, and discuss generalisations to a broader range of structures. Using the findings of this paper, we address the question of wavelength determination in a separate work.[26]

Sections 1 and 2 define the inner Lamé deformation that we simulate, and the isometric model shape used for comparison. In Section 3, we show that the shape and energy of the simulated sheet are consistent with the model. Section 4 addresses our assumptions and discusses the value of such deformations for generating spontaneous structures. Finally, Section 5 gives an account of our numerical methods.

1 Inner Lamé deformation

Given the circular annulus of Fig. 2a, we define the inner Lamé deformation as the equilibrium shape induced by drawing the inner boundary inward by a distance Δ, so that it is forced to live on a cylinder whose radius is reduced by Δ.§ We define the initial inner radius as our unit of length. The pull distance Δ thus acts as the sole loading parameter in the system. The system can thus be conveniently defined using only three geometric parameters: thickness t, the width w, and

‡ For now, we defer the obvious issue of accounting for the observed wrinkle wavelength. Understanding the wrinkle structure seems prerequisite to accounting for the wavelength.

§ As discussed in Section 4, we constrain the inner boundary to move only parallel to the axis of the cylinder.
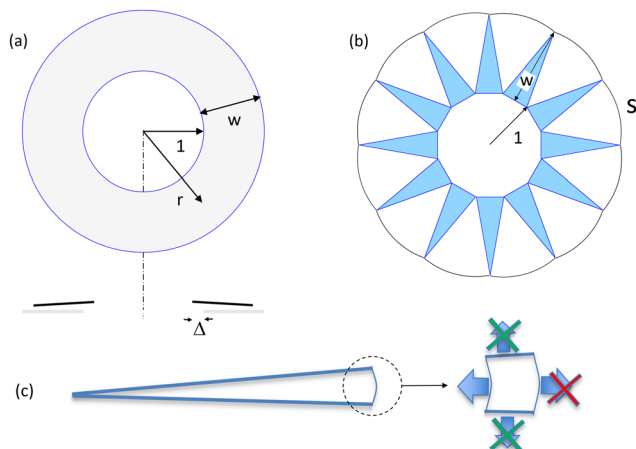
Fig. 2 (a) Sketch of the inner Lamé deformation of a horizontal annulus. (Top) Top view showing the undeformed annulus, of inner radius 1 and width w. (Bottom) Vertical cross-section of the deformed annulus through a line where the vertical displacement of the wrinkle is maximal. The undeformed state is shown in light shading; the dark lines are a section of the deformed annulus, contracted horizontally by a distance Δ. These lines are also displaced upward and tilted downward. (b) Sketch of the circular-cone-triangle construction in its initial, flat state. Here we choose wave-number $m = 6$, hence it has 12 triangles (shown in colour). The mid-line and height w of one triangle are indicated. The sectors bridging the triangles are shown in white; S is its outermost arc length. When the bases of the triangles are moved inward, they must tilt to retain their shape and connectivity. The bridging sectors are squeezed laterally to form cones. A typical deformed example is shown in Fig. 1c. (c) Top view of a narrow sector of the sheet, with detail of an area element at the outer edge of Lamé sheet showing radial (horizontal) and azimuthal (almost vertical) boundary forces. In the fully buckled (FT) regime,[2] the azimuthal forces nearly vanish (as indicated by the upper and lower X's). In the the present "inner Lamé" system, the outer radial force also vanishes, indicated by the X at right. Thus, the inward radial force must also nearly vanish for force equilibrium. All elements to the left of the pictured one are subject to the same argument. Thus except for bending stresses, all radial stresses vanish.

displacement 'loading' Δ. The internal forces determining the shape arise from the bending modulus B and the in-plane stretching modulus Y. Here, we seek the asymptotic behaviour of our annulus in the thin limit: $t \ll w$; $t \ll 1$.

The conventional "FT" reasoning used to explain classical Lamé wrinkling[2] suggests that fine wrinkling like that of Fig. 1. would require negligible radial stretching. In the FT regime, the wrinkling slopes grow to the order of unity, and the associated azimuthal stress becomes negligible compared to the pre-buckling stress. Only the bending azimuthal stress, owing to wrinkling, proportional to the bending modulus and the cur-vature, remains. The same is expected for our inner Lamé case: consider the radial stress in a narrow sector of the annulus (see Fig. 2c). Equilibrium requires that the net radial force on the sector be zero. In the unbuckled state, the inner tension driving the deformation is balanced by the net outward com-ponent of the azimuthal stresses on the sides of the sector. But in the FT regime, this stress is negligible, as argued above. In addition, there is no radial tension at the outer boundary. We conclude that the only forces to balance an inner tension are the weak bending stresses.

The absence of any deformation stress except for bending stress would imply that the sheet deforms only by bending in the thin limit. That is, it is isometric to the undeformed flat annulus. Such an isometric limit can be attained by wrinkles of diverging fineness.[16,17] But if a limiting smooth shape is to exist, then it must obey the geometrical property of "develop-ability". That is, in view of Gauss's Theorema Egregium,[27] there must be a straight generator line through each point of the surface that extends to the boundary without curving in space.[28] In the next sections, we show that the contracted annulus is indeed consistent with a specific developable sur-face, suggested by the numerically determined shape.

2 A developable cone-triangle model

The faceted inner Lamé morphology of Fig. 1 suggests a further hypothesis: that the wrinkled morphology can be seen as a piecewise union of alternating flat triangles and curved conical sectors. We take this as the starting point for our geometric model. For a configuration with wavenumber m, we consider a flat configuration (see Fig. 2b) where the inner boundary is a $2m$-sided polygon. Each segment of this boundary is the base of an isosceles triangle of height w. To complete the annulus, the apexes of adjacent triangles are joined with an arc. The con-structed surface then consists of these triangles and the sectors joining them.

One may readily specify an isometric deformation that allows the inner boundary of this structure to contract. We deform the initial surface by translating the base of each triangle inward toward the centre, specifying that the triangles remain rigid. In order to maintain their shape and connectivity, the triangles must tilt (i.e. rotate about their mid-lines) increasingly as they are drawn inward; adjacent triangles tilt in opposite directions. The sectors connecting two triangles must then also bend in order to remain connected to their triangles. A simple isometric choice for this deformation is to bend the flat sectors into circular conical arcs as the boundaries of each sector squeeze together. These arcs do not in general join smoothly with their adjacent triangles, as further discussed in Section 3.3.

3 Comparing simulated deformation with model

In this section, we test whether the isometric/developable cone-triangle construction is able to predict the quantitative features of our simulated inner Lamé deformation from Section 1. Our finite-element analysis (FEA) software Abaqus uses standard methods to represent the deformed equilibrium shape as the (cylindrical) inner boundary is gradually contracted inward. The inner boundary is allowed to buckle by moving along the cylinder (see Methods). For simplicity we restrict this motion to the axial direction, and allow no azimuthal motion of the boundary points. We describe the effect of this restriction in Section 4.3.4.
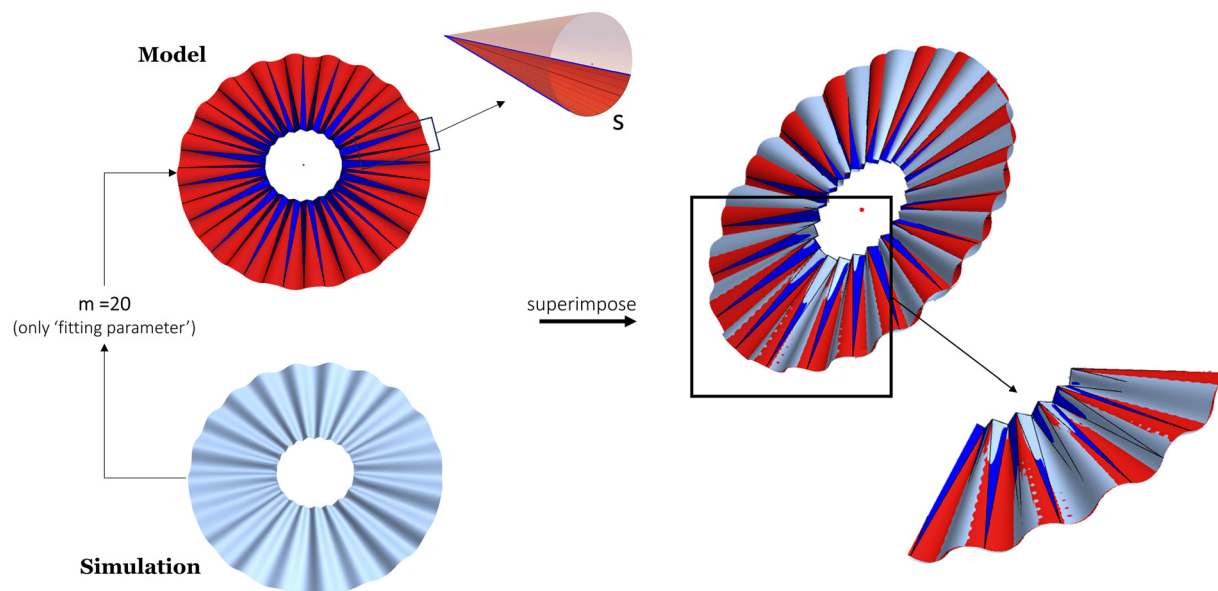
Fig. 3 Qualitative comparison between simulations and our cone-triangle model for a representative sample ($w = 1.67$, $t = 1.33 \times 10^{-3}$). (Left) Given w, Δ and the wavenumber m from the numerical solution, we construct a model cone-triangle solution (cones in red, triangles in blue) using the procedure described in Section 2. (Inset) Zoom-in of a single conical sector (in red) with the entire cone shown (in cream). S marks the length of the outermost arc (as in Fig. 2b) after deformation. For details of construction, see ESI.† (Right) For a qualitative comparison, we superpose the two solutions, with azimuthal rotation as the only degree of freedom. We find close agreement between them; with this top–down view, areas with colour indicate where the model solution is above the numerical solution, while those in grey indicate the opposite. In particular, the zoomed-in boxed portion shows close matching at both inner and outer boundaries. Specifically, the two inner boundaries show a regular zigzag shape of the same amplitude, which extends to qualitatively flat facets and terminates in a smoothly undulating outer boundary that also has similar amplitude in the two sheets. Zooming out to the whole annulus, we see that there is a 'phase mismatch' between the two solutions, with part of the solution in-phase (the boxed region) and part of it out-of-phase. This is due to the non-uniform size of the wrinkles in the numerical solution.

In comparing this calculation to the cone-triangle construction, we must supply two free parameters: the boundary displacement Δ and the wavenumber m. Thus, we record the Δ and m of the finite-element deformation, and then construct the corresponding geometric solution with the same Δ and m. The first comparison we make is purely qualitative – we superpose the two solutions and observe how well they match up. Fig. 3 shows such a comparison, where we have rotated the geometric solution about the cylinder axis to obtain the best superposition. As the figure shows, one may align the two figures so that they overlay well over a significant part of the annulus, with matching zigzags at the inner boundary and matching waves at the outer boundary. Between the inner and outer boundaries, the surfaces match closely enough that the two surfaces alternately hide each other.

The qualitative resemblance seen in the figure encourages a more quantitative comparison. In particular, we propose that for a given wave number m, the shape of the sheet approaches an isometric cone-triangle structure in the limit of zero thickness. Further, approximating each cone as a circular cone sector that connects its neighboring triangles gives a useful match to the shape and energy of the sheet.

Accurate comparison is hindered, however, by the variability of the simulated wrinkles. Though regular in general, the simulated wrinkle pattern is not strictly periodic on the annulus. To optimise the comparison, we perturb the initial flat state of the numerical sheet to promote periodicity. Specifically,

we deform the initial state with a low-amplitude, smooth, periodic wrinkle with a wavelength similar to the original simulations.¶

3.1 Inextensibility and bending strains

We may roughly verify the anticipated isometry of the sheet as announced in the Introduction. To this end, we measure changes in lengths of the material circles at the inner ($r = 1$) and outer ($r = 1 + w$) boundaries.

First, we consider radial inextensibility. Here, we use approximations appropriate for fine buckling and narrow wrinkles as in the far-from-threshold regime of ref. 2. A material circle at radius r in the annulus has fixed initial arc length $L_0(r) = 2\pi r$. After the contraction, this circle deforms into a wavy line, whose horizontal projection is approximately circular under the observed fine buckling. The radius of this contracted circle is the original r plus some radial displacement e_r due to the inward contraction. The fractional change in the projected length L_{xy} is thus given by

$$L_{xy}/L_0 = 1 + e_r/r. \qquad (1)$$

At the inner boundary ($r = 1$), $e_r = -\Delta$ because of the imposed boundary conditions. However, at the outer boundary ($r = 1 + w$), e_r is free to assume any value. If it's different from $-\Delta$, this

---

¶ The initial wrinkle shape chosen is an eigenmode obtained from linear stability analysis performed using the Abaqus software.
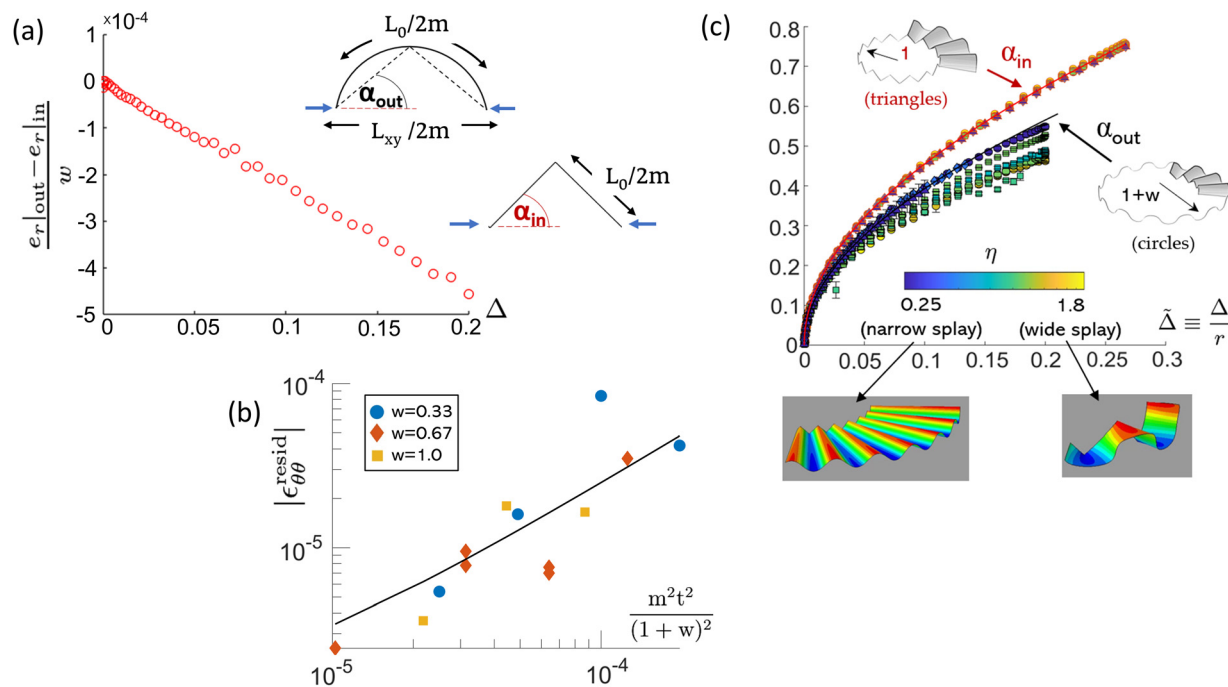
Fig. 4 Comparisons of geometric quantities between theory and simulations (using the explicitly periodic initial conditions described at the beginning of Section 3). (a) Testing radial inextensibility. The graph shows an average radial strain inferred from eqn (1), *i.e.* the small relative difference between the inward displacement at the outer boundary and that at the inner boundary, further discussed in Section 4.3.2. This example had $w = 0.33$, $m = 25$, and $t = 2.67 \times 10^{-4}$. (inset) Sketches of the wrinkle profile at the two boundaries, showing the definition of lengths L_0 and L_{xy}, and slope angles α_{out} and α_{in}. The blue arrows indicate the compression direction. (b) Testing azimuthal inextensibility at the outer boundary. The magnitude of the residual azimuthal strain $|\varepsilon_{\theta\theta}^{resid}|$ recorded slightly inside $r = 1 + w$, plotted logarithmically against the collective variable $m^2 t^2/(1 + w)^2$ at large Δ, for multiple values of m, t and w. The black line shows the linear fit: $|\varepsilon_{\theta\theta}^{resid}| \approx 0.24 \frac{m^2 t^2}{(1 + w)^2}$. (c) Wrinkle slope angle *vs.* applied contraction $\tilde{\Delta} \equiv \Delta/r$ at the inner and outer boundaries (see Section 3.2). (top row) We separately test eqn (3) for α_{in} (in red) and eqn (4) for α_{out} (in black). The simulation data points are plotted alongside the model predictions. Simulated samples of differing width w and wavenumber m are coloured using the dimensionless cone splay parameter, $\eta \equiv \frac{\pi(1 + w)}{mw}$. The error bars are standard deviations from averaging over all the wrinkles. Markers: $w = 0.33$ (circles), $w = 0.67$ (squares), $w = 1.0$ (diamonds), $w = 1.67$ (triangles). (bottom row) Example wrinkle profiles for small and large η: (left) for $\eta = 0.25$ ($w = 1.0$, $m = 25$), and (right) for $\eta = 1.8$ ($w = 0.33$, $m = 7$). Colouring denotes height.

implies the presence of radial strain. In Fig. 4a, we use eqn (1) to provide a simple estimate of the radial strain. For the outer-boundary displacement we infer e_r from eqn (1) and subtract the inner boundary displacement Δ. This gives the change in the horizontal component of the radial length. We interpret this small negative apparent strain in Section 4.3.2.

We may gauge azimuthal extensibility by measuring the full (not projected) change of arc length for the circle at radius r. Here we consider only the outer boundary region. As reported in Fig. 4b, there is a nonzero compression of these circles. This compression reflects the *Elastica* bending stress of pure bending mentioned in Section 1. Specifically, bending at a scale λ produces a residual bending stress, $\sigma_{\theta\theta}^{resid} \sim -B/\lambda^2$, where B is the bending modulus. Thus, from wrinkling of wavenumber m, we expect the outer boundary to have an azimuthal bending *strain* given by:

$$\varepsilon_{\theta\theta}^{resid} \sim -\frac{1}{Y}\frac{B}{\lambda^2} \sim -\frac{m^2 t^2}{(1 + w)^2}, \tag{2}$$

where we have used $\lambda = 2\pi(1 + w)/m$ and $B/Y \sim t^2$ (t is the thickness). The strain $\varepsilon_{\theta\theta}^{resid}$ is calculated for our numerical

samples by directly measuring the change in azimuthal bond lengths along a material circle slightly inside $r = 1 + w$,∥ and then averaging. $\varepsilon_{\theta\theta}^{resid}$ is negative as expected; moreover, it is roughly independent of Δ beyond a transient initial phase. Fig. 4b shows a log–log plot of $|\varepsilon_{\theta\theta}^{resid}|$ for multiple samples with differing values of m, t and w. We see data collapse over the range of a decade, with the predicted slope of unity. We attribute the large variability of the points to variations in the specific wrinkle pattern, which change from one simulation to the next. Based on the linear fit, the estimated pre-factor for eqn (2) is 0.24. We note that this is roughly 50 times greater than the pre-factor calculated theoretically for purely rectangular *Elastica* bending, which gives $\sigma^{resid} = -2B/\lambda^2$.[17] Such a larger value, however, is not unexpected given the inherently two-dimensional nature of our conical *Elastica* arcs.

Fig. 4a and b together provide suggestive evidence for radial and azimuthal inextensibility of the numerical solutions.

∥ This is done to avoid possible strain originating in Gaussian curvature boundary layers at the free outer boundary of the annulus; see ref. 29.

3.2 Evolution of wrinkle amplitude

We now compare specific features of the wrinkle shape to the predictions of the cone-triangle construction. In Fig. 4c, we consider the amplitude of the observed wrinkles. A dimensionless way of measuring the amplitude is by determining the average slope angle α of the wrinkles at the inner and outer boundaries. Though the cone-triangle construction can be implemented for a wide range of wavenumbers m for any given Δ and w, we considered only the narrow range of m that appeared spontaneously in the unperturbed numerics, where $7 \lesssim m \lesssim 35$.[26]

We define the average slope angle α to be the slope angle of the line joining the zero-crossing of the wrinkle with the adjacent maximum (illustrated in inset of Fig. 4a). For angle α_{in} at the inner boundary, the figure explicitly relates α_{in} to L_{xy}/L. For fine wrinkles, we may use eqn (1) to get:

$$\cos \alpha_{in} = 1 - \Delta \equiv 1 - \tilde{\Delta}(1), \tag{3}$$

where we have introduced the reduced variable $\tilde{\Delta}(r) \equiv \Delta/r$. At the outer edge, L_{xy}/L is likewise the ratio of the horizontal line to the arc length of the circular sector (see inset of Fig. 4a). For our circular cone model, it is related to the slope angle α_{out} by

$$\sin 2\alpha_{out}/(2\alpha_{out}) = L_{xy}/L \equiv 1 - \tilde{\Delta}(1 + w). \tag{4}$$

In Fig. 4c, we compare these cone-triangle slope angles to the simulated ones as a function of $\tilde{\Delta}(r)$ for both inner ($r = 1$) and outer ($r = 1 + w$) boundaries. The upper red curve and data points compare α_{in}. The agreement of the data points with the curve confirms that each triangle segment tilts to preserve its length as it is drawn towards the axis. The solid black curve gives the cone-triangle prediction of eqn (4) for α_{out}. The data points on and beneath the curve represent annuli of different widths w and wavenumber m, coloured by their splay: $\eta \equiv \pi(1 + w)/(mw)$. In general, our circular cone model is consistent with the prediction for narrowly-splayed wrinkles, but overestimates the slopes for widely-splayed ones. The pictures below the graph show the annulus shape for different amounts of splay η. They suggest the source of the over-estimated slopes: for the widely splayed example with the greatest discrepancy, the boundary curve is significantly flatter than a circular arc. Thus the simplifying assumptions of our circular-cone construction are not satisfied in this widely-splayed regime.

3.3 Comparing energies

Perhaps the main significance of this isometric deformation is that its energy behaves so differently from that of a generically deformed sheet. It is different in two respects. Firstly, the energy depends only on the bending modulus B, and is independent of the stretching modulus Y for given bending modulus. Secondly, the energy in this limit is qualitatively smaller than for a generic wrinkling deformation with curvature and thickness comparable to our simulations. Below we verify that the energy of the contracted annulus has these distinctive features.

The elastic energy is a sum of strain energy and bending energy:

$$U_{elastic} = U_{strain} + U_{bend}$$

Thus, for a strain-free isometric configuration, we have $U_{elastic} \approx U_{bend}$. For an arbitrary conical deformation extending between lengths L_{min} and L_{max} along the cone axis, the bending energy is given by:

$$U_{bend}^{cone} = \frac{B}{2} \log\left(\frac{L_{max}}{L_{min}}\right) \int ds\, \kappa_N^2, \tag{5}$$

where B is the bending modulus and $\kappa_N(s)$ is the curvature of the outermost arc of the cone normal to the surface, parameterised by the arc length s. For a circular cone as in our model, $\kappa_N(s) = const$. For fine wrinkles,[**] we can write $\kappa_N \approx 1/\rho_c$, where ρ_c is the radius of curvature of the outer circle of the cone (see ESI,† Fig. S2b). Then, adding up the contributions of $2m$ cones for a wrinkled solution of wavenumber m (see ESI,† for details), we get:

$$U_{elastic}^{model}(\Delta) = U_{bend}^{model}(\Delta) \approx B \log\left(\frac{L_{max}}{L_{min}}\right)\frac{\pi(1 + w)w}{\rho_c^2(\Delta)}. \tag{6}$$

Also, in order to avoid high-curvature regions near the inner boundary, where the thin-sheet approximation $\kappa t \ll 1$ becomes questionable, we choose to compare energies for only the outer 3/4th part of the annulus, so that $\log\left(\frac{L_{max}}{L_{min}}\right) = \log(4)$.

In eqn (6) only the quantity $\rho_c(\Delta)$ is not explicitly known. Our circular cone construction (see ESI†) permits us to get an expression for $\rho_c(\Delta)$ in terms of the outer slope angle α_{out}:

$$\rho_c(\Delta) \approx \frac{\pi(1 + w)}{4m}\frac{1}{\alpha_{out}(\Delta)}. \tag{7}$$

We recall that α_{out} depends only on w and Δ, and not on m. Thus $\rho_c \sim 1/m$, and so $U_{elastic}^{model} \sim m^2$, which is the quadratic scaling with wavenumber (at fixed amplitude) expected for a bending energy.

Our primary subject of interest, however, is the scaling of $U_{elastic}^{model}$ with Δ for fixed m. Since $\alpha_{out}(\Delta) \sim \sqrt{\Delta}$ (see Fig. 4c), we expect the squared curvature and the bending energy to scale linearly with Δ: $U_{elastic}^{model} \sim 1/\rho_c^2 \sim \Delta$. We note that this linear form is the same as for the *Elastica* energy of a rod under weak Euler buckling,[30] which is expected since each transverse arc of the cone undergoes Euler buckling with this same Δ dependence.

We may compare this isometric energy with that of conventional wrinkles[17] whose height $h(r,\theta)$ has the separable form $h = f(r)\sin(m\theta)$. As discussed in the ESI,† radial wrinkles of this form have substantial strain ε_c of order of $\varepsilon_c \simeq \Delta/m^2$, much larger than the bending strain of eqn (2), *viz.* $\simeq m^2 t^2$. Accordingly, for fixed Δ and m, the conventional strain ε_c and its associated elastic energy are much larger than their bending counterparts as $t \to 0$. The ESI,† shows that ε_c is also large for the observed m values: $\varepsilon_c \approx 50\varepsilon_B$.

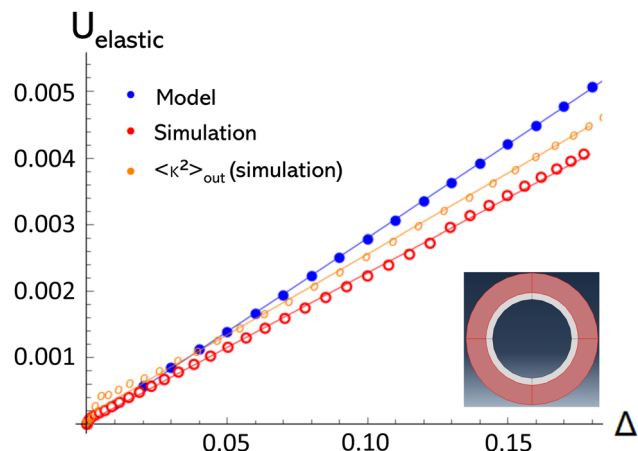** *i.e.* for $\eta \ll 1 \leftrightarrow m \gg \max\{1, 1/w\}$.

Fig. 5 Comparing elastic energies (see Section 3.3) for a representative sample ($w = 1.0$, $m = 25$, $t = 6.67 \times 10^{-4}$): $U_{\text{elastic}}^{\text{sim}}(\Delta)$ (lower curve); (see Methods) with $U_{\text{elastic}}^{\text{model}}(\Delta)$ (upper curve); (eqn (6)) and $U_{\langle \kappa^2 \rangle}^{\text{sim}}(\Delta)$ (middle curve); (eqn (5)). All three curves show *Elastica*-like linear scaling (solid lines are fits), but the two theoretical curves overestimate the simulated energy by roughly 15% and 30% respectively. Other w and m values also generally over-estimated the energies, as discussed in Section 3.3. Energy units are defined in Methods. (inset) Annulus, indicating the region where energies were compared (in red), omitting the high-curvature regions near $r = 1$.

In Fig. 5, we plot three energy curves for a typical sample. These curves compare the simulated energy for a typical example, $U_{\text{elastic}}^{\text{sim}}(\Delta)$ (lower curve), with two theoretical estimates: $U_{\text{elastic}}^{\text{model}}(\Delta)$ (upper curve; see eqn (6)) calculated from our cone-triangle model, and $U_{\langle \kappa^2 \rangle}^{\text{sim}}(\Delta)$ (middle curve) calculated indirectly from the simulated solution through measurement of the mean squared curvature at the outer boundary: $\langle \kappa^2 \rangle_{\text{out}} \equiv \frac{1}{2\pi(1+w)} \int \text{d}s \, \kappa^2$,†† and by using eqn (5). The three curves are similar, differing by a roughly constant factor of order unity. Notably, the full simulated energy including any strain energy, is smaller than the model bending energies. This discrepancy is natural for the circular cone model, since this circular ansatz does not minimise the bending energy. The assumed uniform, circular curvature does not minimize the energy of the cone shape needed in order to bridge between the adjacent triangles. We expect that the system chooses a curvature profile $\kappa(s)$ that minimizes this energy. Thus, as expected, the use of the measured $\kappa(s)$ improves the agreement with the measured energy greatly. But a clear discrepancy remains.

We discuss the possible source of this discrepancy in ESI,† Section S7. It compares the simulated energy profile with that of a conical shape. The mismatch between the two profiles implies that the real surface does not have the straight director lines needed for a developably isometric surface. Such a mismatch requires strain energy. Accordingly, the mismatch should lessen with decreasing thickness. On the other hand this mismatch enables a reduction in bending energy below

that of a cone. Thus the ESI† suggests how a small strain distortion can reduce the total energy below our isometric estimate, as the figure shows.

We conclude that the elastic energy of deformation for the wrinkles encountered in this study is strongly consistent with our claim of an isometric conical deformation. This minimal geometric picture gives a quantitative account of the structure and energy for a given wave number m. Residual discrepancies seem consistent with expected residual stretching effects. Furthermore, the explicit circular-cone-triangle construction gives a workable quantitative estimate of the full elastic energy. This approximation is least accurate when the splay parameter η is large.

4 Discussion

4.1 A developable wrinkling morphology

As shown above, the Lamé radial contraction system is qualitatively altered by removing the outer tension from that system. Specifically, the purely geometric definition of our deformation results in a faceted shape that is in clear contrast to prior force-based deformations.[2,31,32] Our work demonstrates a strong resemblance between the observed shape and the exactly isometric cone-triangle shape defined above. For the numerically feasible thicknesses we report, the cone-triangle hypothesis allows us to reproduce structural and energetic features to good accuracy. Still, detailed analysis shows clear-cut departures from this shape that remain unexplained.

Developable approximations such as the cone-triangle model appear to be a novel approach to describing periodic buckled structures. For the annular contraction deformation studied here, this developable picture seems entirely adequate as an initial quantitative account of the shape. This contrasts with other faceted shapes[33,34] such as twisted ribbons,[35] where a comparable understanding of the energy requires explicit consideration of non-developable geometry and non-bending energy. Our cone-triangle decomposition also provides an instructive example of a buckled shape in a radially symmetric system that does not have the conventional separable form – *i.e.* the buckling displacement is not a product of a radial factor and azimuthal factor.

The developability of the faceted wrinkling structure makes it fundamentally geometric, so that it can be created easily on a computer. This provides a way to programmatically construct smooth radially wrinkled patterns in materials using intrinsically flat components, much in the spirit of origami and other designed materials.[7] In fact, a well-known real-world example of such programmed radial wrinkling is the Elizabethan ruff collar. One way of making a ruff is exactly using the inner Lamé boundary conditions: we take a cloth annulus, and manually make pleats in it such that the inner boundary of the annulus lives on a contracted radius. Fig. 1e and d show, respectively, a ruff collar and its reconstruction using our circular-cone-triangle model; the visual similarity between the two is striking. The conical outer solution seems to capture the ruff wrinkles,

---

†† Here, κ is the arc curvature, without reference to the surface. As before, for fine wrinkles, we have $\kappa \approx \kappa_N$.

in particular their radial straightness and their shape at the outer boundary.

As noted above, accounting for the wrinkles of Fig. 1c is not equivalent to finding a ground-state configuration consistent with the imposed boundary condition. Our deformation was performed quasi-statically, and the wrinkles appeared continuously without abrupt jumps. Thus the system followed a single energy minimum as it deformed. This observed deformation may well have significantly higher energy than the ground state has.

4.2 Nature of the thin-sheet limit

The wrinkles investigated here closely approximate the isometric cone-triangle structure, in both shape and energy, as shown above. That is, many numerical examples with a broad range of thicknesses are well described by a model with no dependence on thickness. We take this as strong evidence that, for a given fine wrinkle number $m \gg \max\{1, 1/w\}$, the sheet approaches this isometric shape as thickness goes to zero. This leaves open the question of how the system selects this m, which clearly does depend on thickness. Given the present understanding of the energy and shape, the groundwork is laid to explain how this wrinkle number is selected. A separate paper by one of us[26] addresses this question.

4.3 Approximations and limitations

4.3.1 Circular cone _Ansatz_. The key modelling assumption used in this paper is the circular _Ansatz_ for the bent cones. As we have shown, this _Ansatz_ serves as a serviceable approximation to the true energy-minimising _Elastica_ solution, while being simple enough to allow for explicit calculation of several key observables, namely, the slope α_{out} and the energy $U_{elastic}$. Section 3 shows that this approximation is accurate only for relatively narrow cones (small η) and large w. This can be partially explained as follows. We expect the circular _Ansatz_ to hold true only for weak Euler buckling. "Weak" here means that the angular squeezing of the cones and the resultant slope, are both small. In the ESI,† we show that this squeezing experienced by a conical sector during deformation increases sharply with decreasing w, such that for our narrowest annuli, it can be as high as 20% for our maximum Δ. At such large values, one no longer expects the weak Euler regime to be valid, and the resultant shape manifests its non-linearity through the flattening apparent in Fig. 4c. We note, however, that even at such large contractions, both the circular _Ansatz_ and the numerical simulations give a linear energy profile, although their slopes are no longer close.

4.3.2 Radial strain. Our main quantitative evidence for isometric wrinkling comes from the azimuthal strain of Fig. 4b and the total energy of Fig. 5. We were not able to obtain comparable quantitative evidence by measuring the radial strain. The nominal radial strain reported in Fig. 4a is of the same order as the azimuthal strain, but it is negative, contrary to expectations. These small strains are significantly affected by further effects that we did not include. One such effect is the vertical slope of the material radial lines.

For example a material line extending radially from the tip of an inner zigzag to the peak of an outer wrinkle undergoes a change of height z from z_{in} to z_{out}. Now, the estimate of Fig. 4a amounts to approximating this line by its horizontal projection, ℓ_{xy}. The full displacement between inner and outer ends of the line is thus $\sqrt{\ell_{xy}{}^2 + (z_{in} - z_{in})^2}$. For the data point in Fig. 4a at $\tilde{\Delta} = 0.2$, this effect adds a correction to the strain of $+0.0002$ to $+0.0003$, greatly reducing the reported value of strain. In addition, the material line is necessarily longer than displacement between its inner and outer ends. Further corrections come from localised strain effects near the inner boundary, as discussed in the next section.

Because of such corrections Fig. 4a shows only a rough consistency with the asymptotic isometry we claim here. For stronger evidence we rely on the energy measurements of Fig. 5.

4.3.3 Inner boundary approximation. Despite this strong resemblance between the simulated wrinkles and the cone-triangle structure, the match cannot be exact. Our construction of the cone-triangle shape in Section 2 required that the inner boundary be a polygon. It is only a good approximation to the simulated circular annulus when the wavelength (_i.e._ $2\pi/m$) is sufficiently small. In particular it must be small in relation to the width w if the triangles are to resemble those of Fig. 1. Details are provided in the ESI,† Section 6.5.

One clear disagreement concerns the length of the inner boundary. In the simulation, the undeformed inner boundary is a circle. Under contraction, each tilted circular arc segment must stretch if it is to remain on the surface of a cylinder. Indeed, we observed such stretching along the inner boundary nodes. However, this stretching zone was confined to this first ring of nodes, with a much weaker stretching in the adjacent ring. In addition, we verified that the associated elastic energy was much smaller than that reported in Fig. 5.

The inexactness of the triangle construction at the inner surface makes it clear that the construction is not a realistic representation of a circular annulus contracted onto a cylinder for _arbitrary_ wavenumber m. We demonstrated the isometric shape for only a limited range of geometries; both the displacement Δ and the width w were confined to moderate ranges. For these moderate conditions the system appears to choose wavelengths fine enough that the inaccuracies of the cone-triangle construction are not important. For more extreme ranges, we expect that the cone-triangle picture shown here will need modification and that the $t \to 0$ limit will be more subtle. In particular, the locally stable isometric structure observed here may give way to macroscopic folding.[23] Finding the conditions in which the cone-triangle wrinkles occur is a fruitful subject for future work.

4.3.4 Lateral constraint boundary condition. As noted in Methods, we prohibit any lateral movement of the nodes on the inner boundary, in order to stabilise the faceted wrinkled regime against folding instabilities. However, even if we do allow lateral movement, we see the same faceted wrinkling at early simulation times, before azimuthal movement of the boundary eventually leads to folding.[23,36] That is, the excess

material concentrates at a single sector along the circumference. Our observations suggest that faceting can be seen for initial buckling, even in the absence of lateral constraints. But our evidence is still only suggestive and needs to be confirmed through physical experiments.

4.4 Application

The deformation geometry treated here amounts to a strategy for avoiding the typical fate of deformed sheets. Such sheets adopt structures that require significant elastic energy beyond the needed bending energy. Often these structures produce uncontrolled disorder, *e.g.* as seen in a crumpled sheet. By contrast, the radial contraction used here guides the sheet into a locally low-energy channel resulting in only bending energy. This low-energy state is moreover attainable by continuous deformation from a flat reference state. Since these deformations lack the additional deformation costs of competing structures, they are intrinsically (locally) stable. They provide a general means to fold and compact a sheet continuously and reversibly with minimal external guidance. We note that the curved inner boundary appears important in stabilising this structure; straight boundaries with no radial contraction[14] do not produce analogous regular wrinkling.

These guiding channels should appear more generally than in the simple circular geometry studied here. The same principles control other inwardly curved boundaries, and other directions of contraction, *e.g.* onto a constraining cone instead of a cylinder.

4.5 Conclusion

While the emergence of developability in wrinkled systems has been studied intensively over the past decade, the simplicity and symmetry of the inner Lamé geometry makes it a particularly clean realisation of such a phenomenon. This faceted morphology is qualitatively different from previously known forms of two-dimensional wrinkling. Significantly, it creates sharply dictated, strongly distorted features with negligible stretching and without a separable radial/azimuthal shape. Moreover, it has many variants to be explored, with real world applications. Finally, this work sets the stage to explain the selection of the wavenumber m.[26]

5 Materials and methods

To investigate the wrinkling morphology of the inner Lamé system, we used the commercial finite-element (FE) solver Abaqus 2018 (SIMULIA, Dassault Systèmes). Using both implicit and explicit dynamic methods‡‡ in a quasi-static regime, we performed simulations of the inner Lamé system using its defining boundary conditions: radial displacement $e_r(r = 1) = -\Delta$ at the inner boundary mesh points, with the outer

---

‡‡ 'Dynamic' means through time integration of the equations of motion. 'Implicit' (using a modified Newton–Raphson method) and 'explicit' refer to the method of integration.

boundary nodes (at $r = 1 + w$) kept free. The maximum value of Δ applied was $\Delta_{max} = 0.267$.

The simulation seeks the configuration that would be attained by adiabatically contracting the inner boundary (*i.e.*, its nodes). Accordingly, it gradually decreases e_r from zero to $-\Delta$ as time t increases from 0 to t_f. The value of t_f is made sufficiently large that the kinetic energy is always a small fraction of the potential energy. Then the final configuration was not noticeably affected by further increase of t_f, as detailed in the ESI.†

To account for the possibility of high strains, the sheet was initially modelled as a Neo-Hookean hyperelastic material with coefficients equivalent to the linear moduli: Young's modulus, $E = 0.907125$ MPa, and Poisson ratio, $\nu = 0.475$ (*cf.* eqn (6)), corresponding to a rubber-like material. The associated bending stiffness B with thickness t is then given by $B = \dfrac{Et^3}{12(1 - \nu^2)}$. To verify that results are independent of the material model, we also re-performed several simulations with a linear material model with these same moduli. Further details on our FEA methods are given in the ESI.†

To test the validity of our results over a range of parameters, we kept the inner radius fixed and varied the other two parameters – width w and thickness t – over the range of a decade. The width w of the annulus was varied between $w = 0.33$ (very narrow) to $w = 1.67$ (moderately wide) – a factor of almost 10. The thickness t was varied between $t = 2.67 \times 10^{-3}$ (thick) to $t = 1.33 \times 10^{-4}$ (very thin), a factor of 20. We performed consistency checks to ensure that the final morphology was independent of the choice of any simulation parameters. For data extraction, we used the software package Abaqus2Matlab.[37]

We used two principal deformation protocols to ensure that the wrinkles we observed were characteristic of the quasi-static limit. Our baseline protocol was done using explicit dynamics, in which the finite elements are accelerated with a constant damping factor. The other deformation protocol used an implicit scheme for integrating the forces, with the damping factor automatically selected by the software to favour quasi-static behaviour. In both cases, to avoid gross kinetic effects, we increased Δ from 0 to Δ_{max} at a rate slow enough such that the kinetic energy of the system always remained $\lesssim 5\%$ of the elastic energy. This is standard procedure for quasi-static analyses in finite-element simulations (see ESI,† for details).

The specifics of the wrinkling morphology depend on how the contracted boundary is constrained. For example, the clamped boundary studied by Mora and Boudaoud[11] leads to a highly compressed boundary layer whose relation to the sheet is difficult to discern. The other extreme is to allow each point on the boundary circle to lie anywhere on the confining cylinder; such boundaries lead to wrinkling only in a transient regime, leading ultimately to collapse into a fold.[23,38] Here we study an intermediate constraint in which points on the bounding circle may move only axially (*i.e.* vertically) on the bounding cylinder; azimuthal (θ) motion is not allowed. Doing so automatically prohibits folding (since this requires lateral motion), but without interfering with the wrinkling.

Author contributions

A. S. P. conceptualised the problem, performed simulations and measurements, and created the majority of the text and figures. L. P. was key in providing numerical support, and in critical readings of several drafts. T. A. W. supervised this work, formulated the cone-triangle model, and helped with conceptualisation, interpretation of data, writing and revising.

Conflicts of interest

There are no conflicts to declare.

Acknowledgements

Notes and references

1 M. Schenk and S. D. Guest, *Proc. Natl. Acad. Sci. U. S. A.*, 2013, **110**, 3276–3281.
2 B. Davidovitch, R. D. Schroll, D. Vella, M. Adda-Bedia and E. A. Cerda, *Proc. Natl. Acad. Sci. U. S. A.*, 2011, **108**, 18227–18232.
3 TrendHunter.com, *Victorian Fashion for Today [Pinterest post], n.d.*, **https://www.pinterest.de/pin/313281717820853822/**, Retrieved March 23, 2023.
4 K. Krieger, *Nature*, 2012, **488**, 146–147.
5 K. Bertoldi, V. Vitelli, J. Christensen and M. van Hecke, *Nat. Rev. Mater.*, 2017, **2**, 17066.
6 C. D. Santangelo, *Ann. Rev. Condens. Matter Phys.*, 2017, **8**, 165–183.
7 S. J. Callens and A. A. Zadpoor, *Mater. Today*, 2018, **21**, 241–264.
8 E. Cerda and L. Mahadevan, *Phys. Rev. Lett.*, 1998, **80**, 2358–2361.
9 E. Cerda and L. Mahadevan, *Phys. Rev. Lett.*, 2003, **90**, 074302.
10 E. Cerda, L. Mahadevan and J. M. Pasini, *Proc. Natl. Acad. Sci. U. S. A.*, 2004, **101**, 1806–1810.
11 T. Mora and A. Boudaoud, *Eur. Phys. J. E*, 2006, **20**, 119–124.
12 M. M. Müller, M. B. Amar and J. Guven, *Phys. Rev. Lett.*, 2008, **101**, 156104.
13 Y. Klein, E. Efrati and E. Sharon, *Science*, 2007, **315**, 1116–1120.
14 H. Vandeparre, M. Piñeirua, F. Brau, B. Roman, J. Bico, C. Gay, W. Bao, C. N. Lau, P. M. Reis and P. Damman, *Phys. Rev. Lett.*, 2011, **106**, 224301.
15 J. Hure, B. Roman and J. Bico, *Phys. Rev. Lett.*, 2012, **109**, 054302.
16 D. Vella, J. Huang, N. Menon, T. P. Russell and B. Davidovitch, *Phys. Rev. Lett.*, 2015, **114**, 014301.
17 B. Davidovitch, Y. Sun and G. M. Grason, *Proc. Natl. Acad. Sci. U. S. A.*, 2019, **116**, 1483–1488.
18 J. D. Paulsen, *Ann. Rev. Condens. Matter Phys.*, 2019, **10**, 431–450.
19 E. Efrati, L. Pocivavsek, R. Meza, K. Y. C. Lee and T. A. Witten, *Phys. Rev. E: Stat., Nonlinear, Soft Matter Phys.*, 2015, **91**, 022404.
20 K. Miura, *The Institute of Space and Astronautical Science Report*, 1985, pp. 1–9.
21 L. Mahadevan and S. Rica, *Science*, 2005, **307**, 1740.
22 J. Kim, J. A. Hanna, R. C. Hayward and C. D. Santangelo, *Soft Matter*, 2012, **8**, 2375.
23 F. Brau, P. Damman, H. Diamant and T. A. Witten, *Soft Matter*, 2013, **9**, 8177.
24 R. Levien, *The elastica: a mathematical history*, Technical Report, 2008.
25 E. Cerda and L. Mahadevan, *Proc. R. Soc. A*, 2005, **461**, 671–700.
26 A. S. Pal, *Soft Matter*, 2023, **19**, 5551–5559.
27 M. P. do Carmo, *Differential Geometry of Curves & Surfaces*, Prentice Hall, 1976.
28 S. C. Venkataramani, T. A. Witten, E. M. Kramer and R. P. Geroch, *J. Math. Phys.*, 2000, **41**, 5107–5128.
29 E. Efrati, E. Sharon and R. Kupferman, *Phys. Rev. E: Stat., Nonlinear, Soft Matter Phys.*, 2009, **80**, 016602.
30 B. Audoly and Y. Pomeau, *Elasticity and geometry*, OUP, Oxford, 2010.
31 J. Huang, M. Juszkiewicz, W. H. de Jeu, E. Cerda, T. Emrick, N. Menon and T. P. Russell, *Science*, 2007, **317**, 650–653.
32 M. Piñeirua, N. Tanaka, B. Roman and J. Bico, *Soft Matter*, 2013, **9**, 10985.
33 T. A. Witten, *Rev. Mod. Phys.*, 2007, **79**, 643–675.
34 K. A. Seffen and S. V. Stott, *J. Appl. Mech.*, 2014, **81**, 061001.
35 H. Pham Dinh, V. Démery, B. Davidovitch, F. Brau and P. Damman, *Phys. Rev. Lett.*, 2016, **117**, 104301.
36 J. D. Paulsen, V. Démery, K. B. Toga, Z. Qiu, T. P. Russell, B. Davidovitch and N. Menon, *Phys. Rev. Lett.*, 2017, **118**, 048004.
37 G. Papazafeiropoulos, M. Muñiz-Calvente and E. Martnez-Pañeda, *Adv. Eng. Software*, 2017, **105**, 9–16.
38 L. Pocivavsek, R. Dellsy, A. Kern, S. Johnson, B. Lin, K. Y. C. Lee and E. Cerda, *Science*, 2008, **320**, 912–916.